
DUST2MSG

# DUST2MSG - Product Validation Report V1

Prepared by : M. Luffarelli, L. Franceschini and Y. Govaerts (Rayference)
Reference : DUST2MSG-PVR
Version : V1.0
Date : 02/10/2023

RAYFERENCE

# Distribution List

Author(s) : Marta Luffarelli, Lucio Franceschini and Yves Govaerts

Reviewers (s) : Simon Pinnock

# Document Change Record

| Doc. Version | Date | CISAR Release | Remarks |
|---|---|---|---|
| Version 1.0 | September 2023 | 2.2.11 | - |

# Table of Contents

**Distribution list** i

**Document Change Record** i

**Table of Contents** i

**List of Acronyms** iv

**1 Introduction** 1

1.1 Purpose . . . 1
1.2 Scope . . . 1
1.3 Reference Documents . . . 1

**2 Validation Methodology** 2

**3 Validation results** 3

3.1 Validation against CAMS and MODIS datasets . . . 3
3.2 Validation against ground-based measurements . . . 4
3.2.1 Uncertainty evaluation . . . 10
3.3 Aerosol-cloud interactions . . . 12
3.4 AOD/COD impact on surface downward flux . . . 14

**4 Case Study** 15

4.1 The Godzilla dust storm . . . 15

**5 Known issues and algorithm limitations** 18

5.1 Corrupted SEVIRI image . . . 18
5.2 Ocean color . . . 18
5.3 Snow pixels . . . 18

**6 Summary** 20

# List of Figures

1 Products over over the processed common area between MSG1 and MSG4: true color image obtained from the MODIS MOD09GA product (a); SEVIRI/CISAR combined AOD/COD retrieval (b), MODIS/MAIAC MCD19A2 product (c) and CAMS dataset (d). . . . 3

2 Location of the selected AERONET stations. The color-code indicates the percentage of CISAR retrieval satisfying the GCOS Threshold requirements. . . . 4

3 Absolute relative error, calculated as $|\frac{\tau_{CISAR} - \tau_{AERONET}}{\tau_{AERONET}}|$, in function of the scattering angle $g$. . . . 4

4 Density plot associated to the AOD at 550nm retrieved by CISAR (y axis) against AERONET (x axis). The black solid line represents the 1:1 line, the black dotted line represent the Threshold GCOS requirements: max(0.06, 0.2*AOD). . . . 5

5 Variation of RMSE (left y axis) and percentage of points satisfying the GCOS requirements (right y axis) with respect to the QI (x asis). . . . 6

6 Time series of the daily AOD at $550\,\mathrm{nm}$ retrieved by SEVIRI-CISAR (orange), MODIS-MAIAC (blue) and provided by AERONET (black) between April 15th and May 15th 2020 over Nicosia, Cyprus. . . . 6

7 Products over over Cyprus during May 1st, 2020: true color image obtained from the MODIS MOD09GA product (a); SEVIRI/CISAR combined AOD/COD retrieval (b), MODIS/MAIAC MCD19A2 product (c) and CAMS dataset (d). . . . 7

8 Time series of the daily AOD at $550\,\mathrm{nm}$ retrieved by SEVIRI-CISAR (orange) and provided by AERONET (black) between March and September 2020 over Rome, Italy. 8

9 Same as 8 but over Qena, Egypt. . . . 8

10 FMF bias between the CISAR product the AERONET spectral de-convolution algorithm (SDA) dataset (blue) as a function of the total AERONET AOD at $500\,\mathrm{nm}$. The vertical bars represent the standard deviation in each bin. The dashed line represent a bias of $\pm$ 10%. Only CISAR retrievals with a QI higher than 0.6 are considered. . . . 9

11 FMF daily time series over Qena, Egypt, obtained from CISAR retrieval (solid orange line) and AERONET (dashed black line). . . . 9

12 CISAR retrieved micro-physical aerosol properties retrieved over Qena, Egypt, in the 2D CISAR solution space (blue triangle), bounded by the aerosol vertices associated with fine non-absorbing (FN), fine absorbing (FA) and coarse particles (C). The color code reports the FMF associated to each retrieval. . . . 10

13 Normalised error CDF (a), PDF (b) and expected AOD discrepancy against percentiles of absolute AOD retrieval error (c) over selected AERONET stations. The shaded grey area represent the ideal case where the normalised AOD error can be approximated as a Gaussian distribution with mean 0 and variance 1. . . . 12

14 Density plot between the water cloud radius (y axis) and the fine mode AOD (x axis) during May 2020 over Europe obtained with the CISAR algorithm applied to SEVIRI observations. . . . 13

15 Density plot between the water cloud radius (y axis) and the fine mode AOD (x axis) during May 2020 over Europe obtained with the CISAR algorithm applied to SEVIRI observations. . . . 13

16 Combined AOD/COD product at 550 nm (16a) and surface downward flux in the VIS0.6 band (16b) retrieved with the CISAR algorithm applied to SEVIRI observations on-board MSG1 and MSG4 during June16th, 2020. . . . 14

17 Density plot between the surface downward fluxes in the SEVIRI VIS0.6 band (y axis) and the total OD retrieved at $0.55\,\mathrm{um}$ (x axis) during May 2020 over Europe obtained with the CISAR algorithm applied to SEVIRI observations. . . . 15

18 Products over over the West African coast during June 16th, 2020: true color image obtained from the MODIS MOD09GA product (a); SEVIRI/CISAR combined AOD/COD retrieval (b), MODIS/MAIAC MCD19A2 product (c) and CAMS dataset (d). . . . 16

19 Fine Mode Fraction retrieved from the CISAR algorithm applied to SEVIRI (19a), from MAIAC applied to MODIS (19b) and the associated bias (19c). . . . 17

20 Time series during June 2020 of the daily average of the Coarse Mode AOT (left y axis, blue line) and the surface downward irradiance (right y axis, red line) retrieved by CISAR. . . . 18

21 Level 1.5 image acquired by MSG1 in the VIS0.6 band (a) and associated CISAR AOD/COD retrieval at $0.55\,\mathrm{um}$ (b) during May 9th 2020. . . . 19

# List of Acronyms

| | |
|---|---|
| AERONET | Aerosol Robotic Network |
| AOD | Aerosol Optical Depth |
| BHR | BiHemispherical Reflectance |
| BRF | Bidirectional Reflectance Factor |
| CCN | Cloud Condensation Nucleii |
| CDF | Cumulative Density Function |
| CISAR | Combined Inversion of Surface and AeRosol |
| CM | Coarse Mode |
| COD | Cloud Optical Depth |
| ECV | Essential Climate Variable |
| ESA | European Space Agency |
| FM | Fine Mode |
| GCOS | Global Climate Observing System |
| GEDAP | GEneric DAta Processing Chain |
| LTDR | Long Term Data Record |
| MAIAC | Multi-Angle Implementation of Atmospheric Correction |
| OE | Optimal Estimation |
| PDF | Probability Density Function |
| PVR | Product Validation Report |
| QI | Quality Indicator |
| RTM | Radiation Transfer Model |
| TOA | Top Of Atmosphere |

# 1 Introduction

## 1.1 Purpose

The purpose of this Product Validation Report (PVR) is to evaluate the DUST2MSG User Products delivered by the GEDAP-CISAR algorithm [RD1, RD2] against ground based measurements, models and cross-sensors retrieval.

## 1.2 Scope

GEDAP primary objective is to feed the CISAR algorithm with the data needed to perform the inversion of a physically-based Radiative Transfer Model (RTM) and to generate Earth system components products based on these retrievals in standard format.

## 1.3 Reference Documents

| | |
|---|---|
| RD1 | Govaerts, Y. and Luffarelli, M. (2018) “Joint retrieval of surface reflectance and aerosol properties with continuous variations of the state variables in the solution space: Part 1: theoretical concept”, Atmospheric Measurement Techniques, 11, no. 12, 6589–6603. |
| RD2 | Luffarelli, M. and Y. Govaerts. (2019). “Joint Retrieval of Surface Reflectance and Aerosol Properties with Continuous Variation of the State Variables in the Solution Space – Part 2: Application to Geostationary and Polar-Orbiting Satellite Observations." Atmospheric Measurement Techniques 12 (2): 791–809. |
| RD3 | Luffarelli, M., Govaerts, Y. and Franceschini, L. (2022) "Aerosol Optical Thickness Retrieval in Presence of Cloud: Application to S3A/SLSTR Observations." Atmosphere 2022, 13, 691. https://doi.org/10.3390/atmos13050691 |

# 2 Validation Methodology

The validation of the retrieval obtained with CISAR algorithm applied to SEVIRI observations acquired between March and August 2020 is performed by comparison with ground-based measurements (AERONET), cross-sensors products (MODIS) and model-based datasets (CAMS). The AERONET stations are selected for the validation exercise against ground-based measurements based on criteria of surface homogeneity and data availability of AERONET V3 Level2.0 (Giles et al. 2017). AERONET observations are collocated within a $\pm$ 30 minutes window, to account for the different spatial resolution, as SEVIRI images are processed at 10 km pixel resolution. The MODIS product against which the CISAR retrieval is evaluated is chosen between the Dark Target algorithm (MOD04, Vermote 2021) and the MAIAC algorithm (MCD19A2, Lyapustin 2018), depending on data availability.

CISAR performances against the reference dataset are evaluated in terms of temporal evolution (assessed through time series), correlation, Root Mean Square Error (RMSE) and percentage of points satisfying the Global Climate Observing System (GCOS) requirements for Essential Climate Variables (ECV) (WMO 2022). The GCOS requirements are classified as Threshold, Breakthrough and Goal; statistics are calculated for each of the three cases, discussing possible reasons why some retrievals do not satisfy the requirements. The capability of the CISAR algorithm to follow the temporal evolution of the aerosol load will also be assessed through time series and compared with the AERONET product. The retrieval pixel-level uncertainty are also evaluated following the method proposed by Sayer et al. 2020.

CISAR aerosol product is delivered in the vicinity and in presence of thin clouds; such combined product offers the possibility to observe mutual aerosol-cloud interactions. CISAR product will be analysed to verify the observation of the aerosol first indirect effect from satellite observations (Twomey 1974) as well the aerosol swelling in the humid environment surrounding clouds (Quaas et al. 2010). Finally, it will be evaluated how the total optical depth (OD) reduces the amount of solar downward irradiance measured by CISAR in SEVIRI spectral bands. The case study of the Godzilla dust storm, taking place in June 2020 and originating at the west coast of Sahara will be evaluated.

# 3 Validation results

## 3.1 Validation against CAMS and MODIS datasets

The DUST2MSG product is visually evaluated against other sensors product (MODIS) as well as against model dataset (CAMS). Figure 1 shows good agreement in terms of spatial distribution of aerosols among all datasets. In the Sahara and Sahel regions dust events can be observed in the three datasets. The presence of clouds in a large portion of the image, visible in the RGB image obtained from MODIS MOD09GA observations (Vermote 2021), highlights the increased aerosol spatial coverage obtained with the CISAR algorithm compared to MODIS/MAIAC, both over land and water; this is thanks to CISAR's capabilities of processing all-skies and retrieving aerosols and clouds within the same pixel. The potential impact of such combined product in aerosol-cloud interactions studies will be discussed in Section 3.3. CISAR capability to retrieve severe dust storm as coarse particles is evaluated in Section 4.1 in the case of the Godzilla dust storm in June 2020.

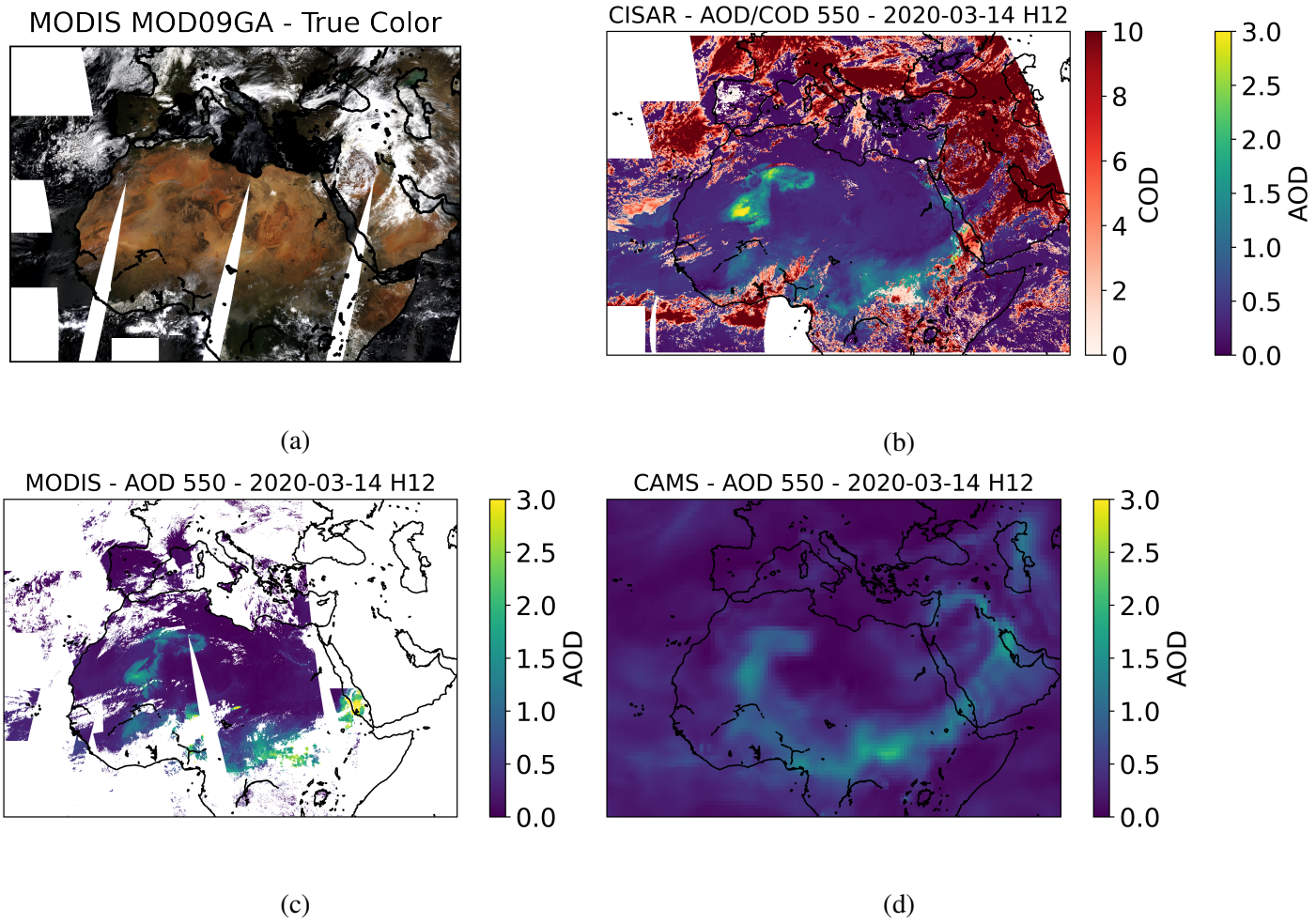


Figure 1: Products over over the processed common area between MSG1 and MSG4: true color image obtained from the MODIS MOD09GA product (a); SEVIRI/CISAR combined AOD/COD retrieval (b), MODIS/MAIAC MCD19A2 product (c) and CAMS dataset (d).

## 3.2 Validation against ground-based measurements

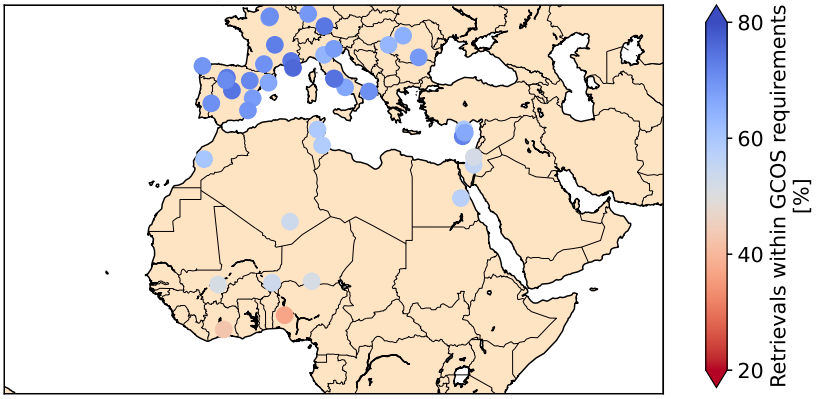


Figure 2: Location of the selected AERONET stations. The color-code indicates the percentage of CISAR retrieval satisfying the GCOS Threshold requirements.

The CISAR AOD product is here evaluated against AERONET L2.0 V3 dataset. Figure 2 shows all the AERONET stations considered in the evaluation exercise, based on surface homogeneity and data availability in the period process within this project (March-August 2020). The color code in Figure 2 shows the percentage of CISAR retrieval satisfying the GCOS threshold requirements. It can be seen that CISAR performances vary between Europe and North Africa, where the surface is brighter and this decreases the contrast between the contribution at the satellite from the surface and from the atmosphere, reducing the associated information content. The performances of the CISAR algorithm evaluated against AERONET measurements depend on the observation geometry as well. Luffarelli et al. 2016 demonstrated that the information content associated to geostationary observation is subject to both daily and seasonal variations. This finding is confirmed within this study, with the absolute relative error strongly increases towards the backscattering direction, reaching

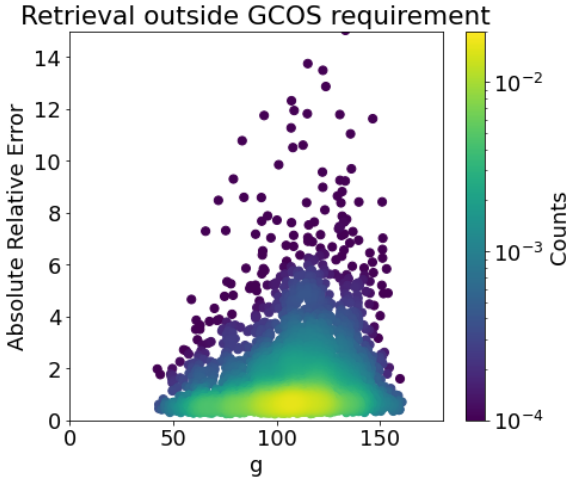


Figure 3: Absolute relative error, calculated as $|\frac{\tau_{CISAR} - \tau_{AERONET}}{\tau_{AERONET}}|$, in function of the scattering angle $g$.

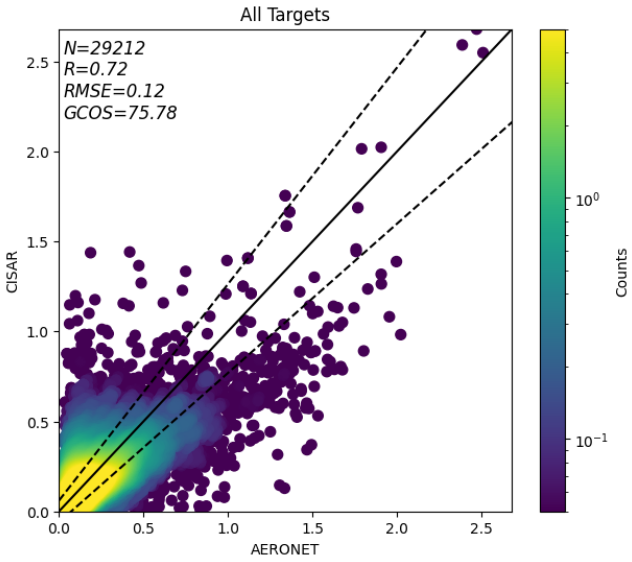


Figure 4: Density plot associated to the AOD at 550nm retrieved by CISAR (y axis) against AERONET (x axis). The black solid line represents the 1:1 line, the black dotted line represent the Threshold GCOS requirements: max(0.06, 0.2*AOD).

maximum values at scattering angles in the range of 100°-140° (Figure 3). This range corresponds to the minimum of the aerosol phase function, where little information content on the aerosols is available and the discrimination between the fine and coarse mode is particularly challenging (Fougnie et al. 2020).

The overall evaluation over the selected targets is shown in Figure 4. CISAR product is evaluated in terms of correlation coefficient, Root Mean Square Error (RMSE) and percentage of points satisfying the GCOS requirements. CISAR retrievals with Quality Indicator (QI) lower than 0.2 are not considered in this exercise (Luffarelli and Govaerts 2019). The GCOS requirements for the AOD are reported in Table 1. Figure 5 shows the variation in RMSE and percentage of points satisfying the GCOS requirements according to the QI; it can be seen that the performances of the CISAR algorithm strongly improve selecting retrieval with increasing QI. The user can thus filter the retrieval according to the relevant application.

Among the retrievals that are over-estimated by CISAR with respect to AERONET, 54% are associated to values of AOD lower than 0.2. This suggests that some residual cloud contamination might affect the aerosol retrieval from satellite, as the likelihood of cloud contamination in satellite products

Table 1: GCOS requirement for the AOD ECV and percentage of CISAR retrieval within the requirements.

| | Requirements | % within requirements |
|---|---|---|
| Threshold | 20% or 0.06 | 75.78 |
| Breakthrough | 10% or 0.04 | 42.51 |
| Goal | 4% or 0.02 | 25.29 |

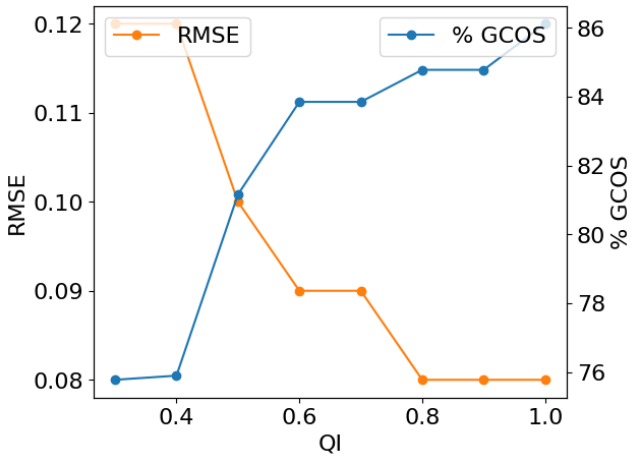


Figure 5: Variation of RMSE (left y axis) and percentage of points satisfying the GCOS requirements (right y axis) with respect to the QI (x asis).

increases at coarser resolution (Remer et al. 2012). Limiting the collocation between CISAR retrieval and AERONET observations to cases where all AERONET observations are available decreases the occurrence of overestimated retrieval from 10.6% to 8.8%, while the decrease in occurrences of underestimation is only 0.3%; this is in line with the assumption that the overestimation at low AODs comes partially from cloud contamination, as a missing AERONET observation can suggest the presence of clouds. Aerosol particles near clouds become more hydrating and swell in size, resulting in increased AOD (Quaas et al. 2010). The increased AOD might be observed by the satellite but undetected by ground-based measurements given the different spatial resolution.

An example of this issue can be observed over Nicosia, Cyprus, during May 2020 (Figure 6). Dur-

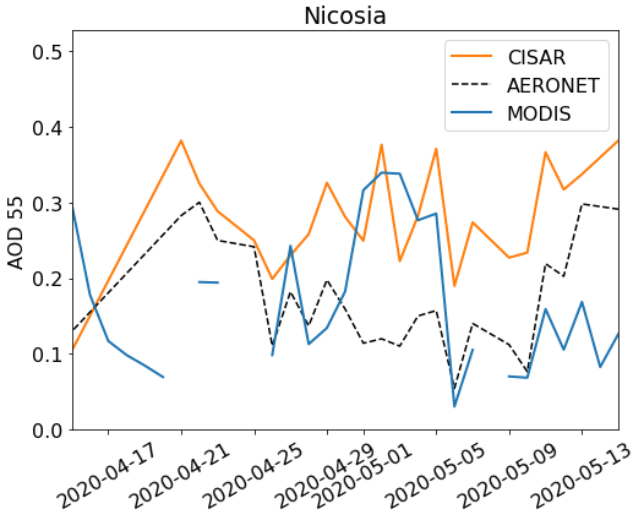


Figure 6: Time series of the daily AOD at 550 nm retrieved by SEVIRI-CISAR (orange), MODIS-MAIAC (blue) and provided by AERONET (black) between April 15th and May 15th 2020 over Nicosia, Cyprus.

ing the first 5 days of May, both CISAR applied to SEVIRI observations and MAIAC applied to MODIS observations (Lyapustin 2018) show overestimation compared to AERONET. Looking at the true color satellite image obtained from MODIS MOD09GA (Vermote 2021) and at the combined AOD/COD product obtained with CISAR applied to SEVIRI images (Figure 7a and b), it can be seen that the the island of Cyprus appears to be cloudy; the CISAR algorithm can correctly retrieve the position of clouds. Compared to the MAIAC algorithm applied to MODIS (Lyapustin and Wang 2018) in Figure 7c, the spatial coverage of the aerosol product is improved, as the CISAR products extends to the vicinity of clouds. Unfortunately, MODIS/Terra is in sun glint conditions during May 1st, 2020, therefore a large portion of the image is not processed; however, the improved spatial coverage with the CISAR algorithm can still be observed in the Western part of the observed area and in the Northern part of Syria. The artefacts over the Nile region in the MODIS image likely results from the composite of different orbits. The MODIS MCD19A2 (Lyapustin 2018) product presents lower AOD values than CISAR all over the image; however, comparison with the CAMS dataset (Inness et al. 2019) shown in Figure 7d suggests that the magnitude of the AOD is larger than the MODIS/MAIAC

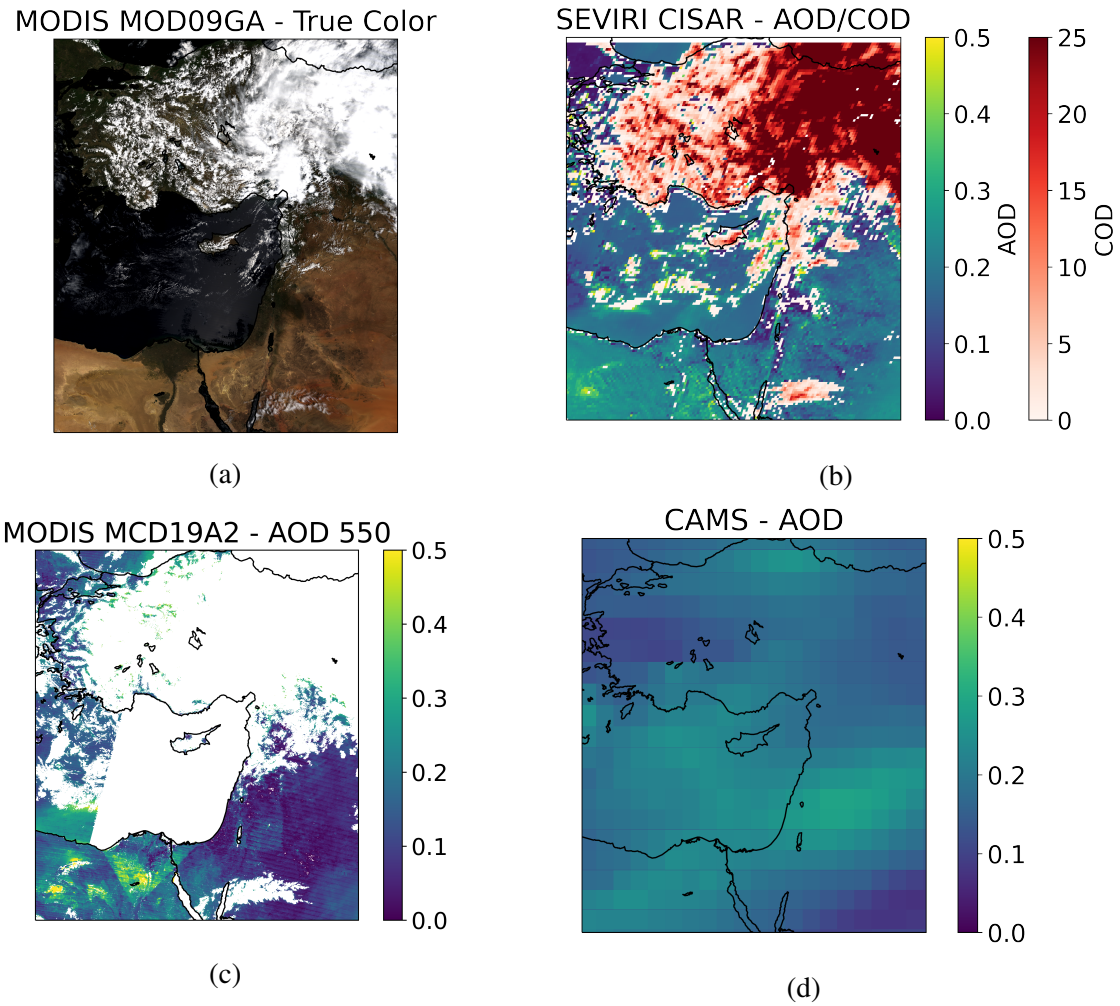


Figure 7: Products over over Cyprus during May 1st, 2020: true color image obtained from the MODIS MOD09GA product (a); SEVIRI/CISAR combined AOD/COD retrieval (b), MODIS/MAIAC MCD19A2 product (c) and CAMS dataset (d).

retrieval.

Despite the limitations related to residual cloud contamination and to the different spatial resolution between ground based observations and satellite retrievals, the CISAR algorithm shows high correlation against the AERONET dataset. Figure 8 and 9 show an example of daily AOD time series retrieved over Rome, Italy, and over Qena, Egypt, from CISAR and AERONET; the two datasets show good consistency in terms of temporal evolution of the AOD, although CISAR tends to slightly underestimate larger values of AOD. The time series over Qena is limited to the March-May time frame due to little availability of AERONET data between June and September.

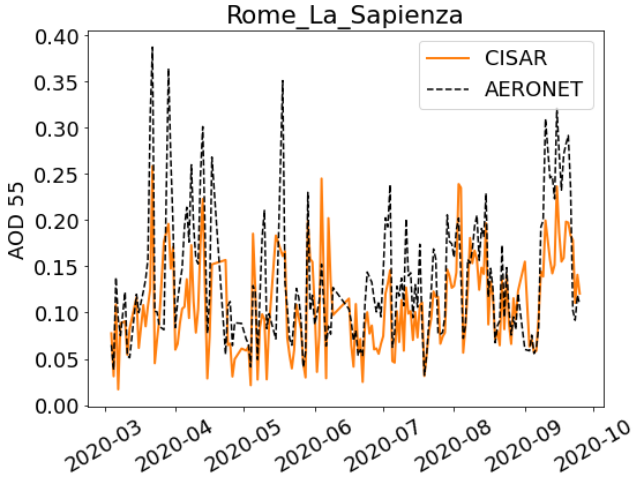


Figure 8: Time series of the daily AOD at 550 nm retrieved by SEVIRI-CISAR (orange) and provided by AERONET (black) between March and September 2020 over Rome, Italy.

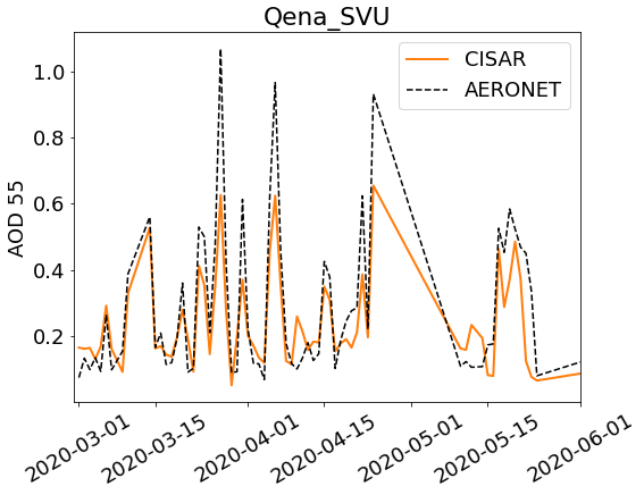


Figure 9: Same as 8 but over Qena, Egypt.

Finally, the CISAR capability of retrieving correctly the Fine Mode (FM) fraction has been evaluated against AERONET spectral de-convolution algorithm (SDA) product (O'Neill et al. 2003). It should be noted that an approximation is introduced as the SDA product is available at 500 nm while the

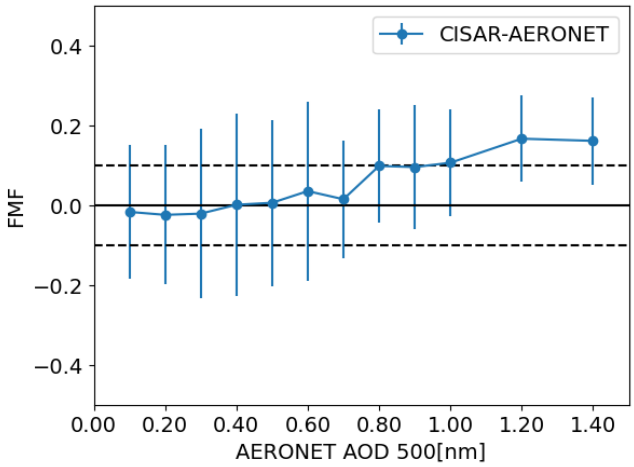


Figure 10: FMF bias between the CISAR product the AERONET spectral de-convolution algorithm (SDA) dataset (blue) as a function of the total AERONET AOD at 500 nm. The vertical bars represent the standard deviation in each bin. The dashed line represent a bias of ± 10%. Only CISAR retrievals with a QI higher than 0.6 are considered.

CISAR AOD is delivered at 550 nm. The FM Fraction (FMF) is calculated for both AERONET and CISAR; the associated bias is plotted as a function of the total AERONET AOD at 500 nm in Figure 10. The two products show similar magnitude and behaviour for AOD lower than 0.8. At higher values, CISAR seems to retrieve a higher FMF with respect to AERONET, suggesting that CISAR might underestimate the coarse mode contribution at high values of AOD. This can be observed as well in Fig. 11, showing the FMF daily-averaged time series over Qena, Egypt, obtained from CISAR and AERONET respectively. Comparing Fig. 11 with Fig. 9, it can be seen that AERONET shows lower values of FMF at larger values of AOD, while CISAR shows a different behaviour (see for

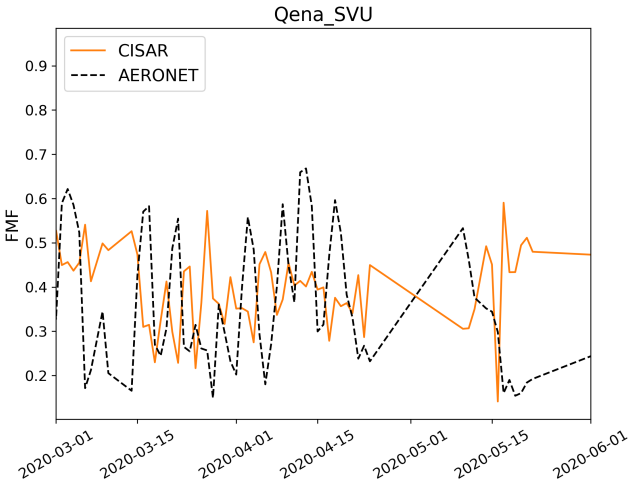


Figure 11: FMF daily time series over Qena, Egypt, obtained from CISAR retrieval (solid orange line) and AERONET (dashed black line).

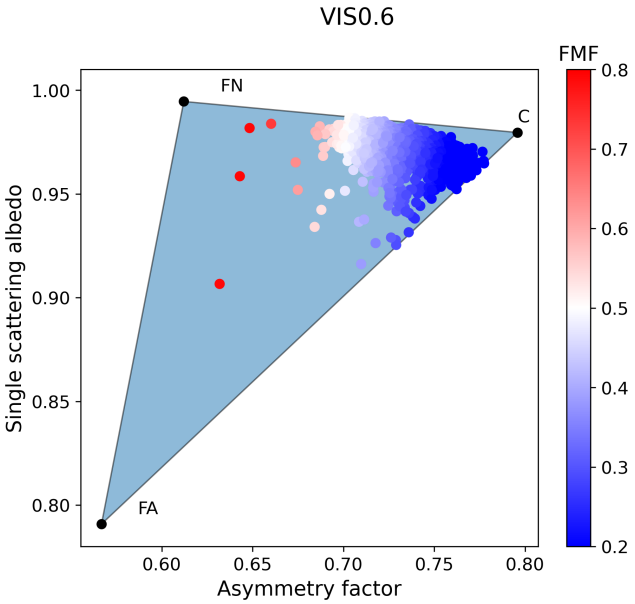


Figure 12: CISAR retrieved micro-physical aerosol properties retrieved over Qena, Egypt, in the 2D CISAR solution space (blue triangle), bounded by the aerosol vertices associated with fine non-absorbing (FN), fine absorbing (FA) and coarse particles (C). The color code reports the FMF associated to each retrieval.

instance the time window between end of April - beginning of May). However, CISAR Coarse Mode (CM) AOD refers to the single coarse mode vertex used to bound the atmospheric solution space (Luffarelli and Govaerts 2019). fThis concept can be visualised in Fig. 12, showing the CISAR retrieved micro-physical aerosol properties in the 2D CISAR solution space, computed as in Eq. 2 in Luffarelli et al. 2022. As there is only one coarse vertex at the moment with specific properties, in order to have different radiative properties, e.g. larger absorption, it is necessary to increase the OT associated with the fine-mode vertices, thus resulting in a larger FMF.

### 3.2.1 Uncertainty evaluation

The Optimal Estimation (OE) framework within which the inversion is performed delivers pixel-level retrieval uncertainties for each state variable $\mathbf{x}$, assuming a linear behaviour in the vicinity of the solution (Rodgers 2000). Under this condition, the retrieval uncertainty is determined by the shape of the cost function $J(\mathbf{x})$ at the solution $\hat{\mathbf{x}}$ through the second derivative:

$$\sigma^2_{\hat{\mathbf{x}}} = \left( \frac{\partial^2 J(\mathbf{x})}{\partial \mathbf{x}^2} \right)^{-1} \tag{1}$$

Equation 1 is applied to all the state variables (surface parameters, optical depth associated to each atmospheric vertex). The uncertainty associated to any quantity $y(\mathbf{x})$ obtained from the state variables

(e.g. total AOD) is computed considering the cross correlation terms (100:2008 2008, Eq. 13):

$$\sigma_{\mathbf{y}}^2 = \sum_i \left[ \left( \frac{\partial y(\mathbf{x})}{\partial \mathbf{x_i}} \right)^2 \sigma_{\mathbf{x_i}}^2 \right] + \sum_i \sum_{j \neq i} \left[ \left( \frac{\partial y(\mathbf{x})}{\partial \mathbf{x_i}} \right) \left( \frac{\partial y(\mathbf{x})}{\partial \mathbf{x_j}} \right) \sigma_{\mathbf{x_i},\mathbf{x_j}} \right]. \tag{2}$$

CISAR retrieval uncertainties are evaluated following the method proposed in Sayer et al. 2020, comparing the retrieved uncertainty to the ideal case, where the normalised error $\Delta N$ can be approximated by a Gaussian distribution with mean $0$ and variance $1$. The normalised error $\Delta N$ is defined as follows:

$$\Delta N = \frac{\tau_S - \tau_A}{\sqrt{\epsilon_S^2 - \epsilon_A^2}}. \tag{3}$$

Sayer et al. 2020 then evaluates the uncertainties by means of the Probability Density Function (PDF) and Cumulative Density Function (CDF) to assess the overall magnitude of retrieval errors compared to expectations as well as the presence of an overall bias against AERONET observations. Additionally, a quantile analysis provide information on the validity of the uncertainty estimates across the range of estimated uncertainty. Match-ups with AERONET are considered within a $\pm 15$ minutes windows and are filtered according to the number of available AERONET data points and standard deviation in the selected time window.

Figure 13 shows the results of the uncertainty evaluation exercises the three stations available both in the present dataset and in Sayer et al. 2020 (Ilorin, Venice and Palencia) as well as the AERONET stations in Rome and Qena presented in Section 3.2. Results confirm that CISAR mostly overestimates the retrieval uncertainties, *i.e.* the actual error is smaller than the expected discrepancy. The only exception to this is represented by the station of Ilorin, selected as test case by Sayer et al. 2020 given the complexity of its aerosol optical properties, which are more absorbing than assumed by many retrieval algorithms and show large heterogeneity, where CISAR's uncertainties predict a smaller error. However, looking more in detail in the percentile analysis (Figure 13c), it can be seen that the expected discrepancy generally increases with retrieval error; this represents a significant improvement compared to Sayer et al. 2020, especially visible over the sites of Palencia and Venice. From Fig. 13b it can also be observed that for all stations, to the exception of Ilorin, the normalised error median value is very close to $0$ ($< 0.41$. The overestimation of the uncertainties could partially originate from the large uncertainty on the prior information used in CISAR, as this is obtained from a climatology which delivers the aerosol optical thickness annual mean per aerosol type (coarse, fine absorbing, fine non-absorbing) (Kinne et al. 2013).

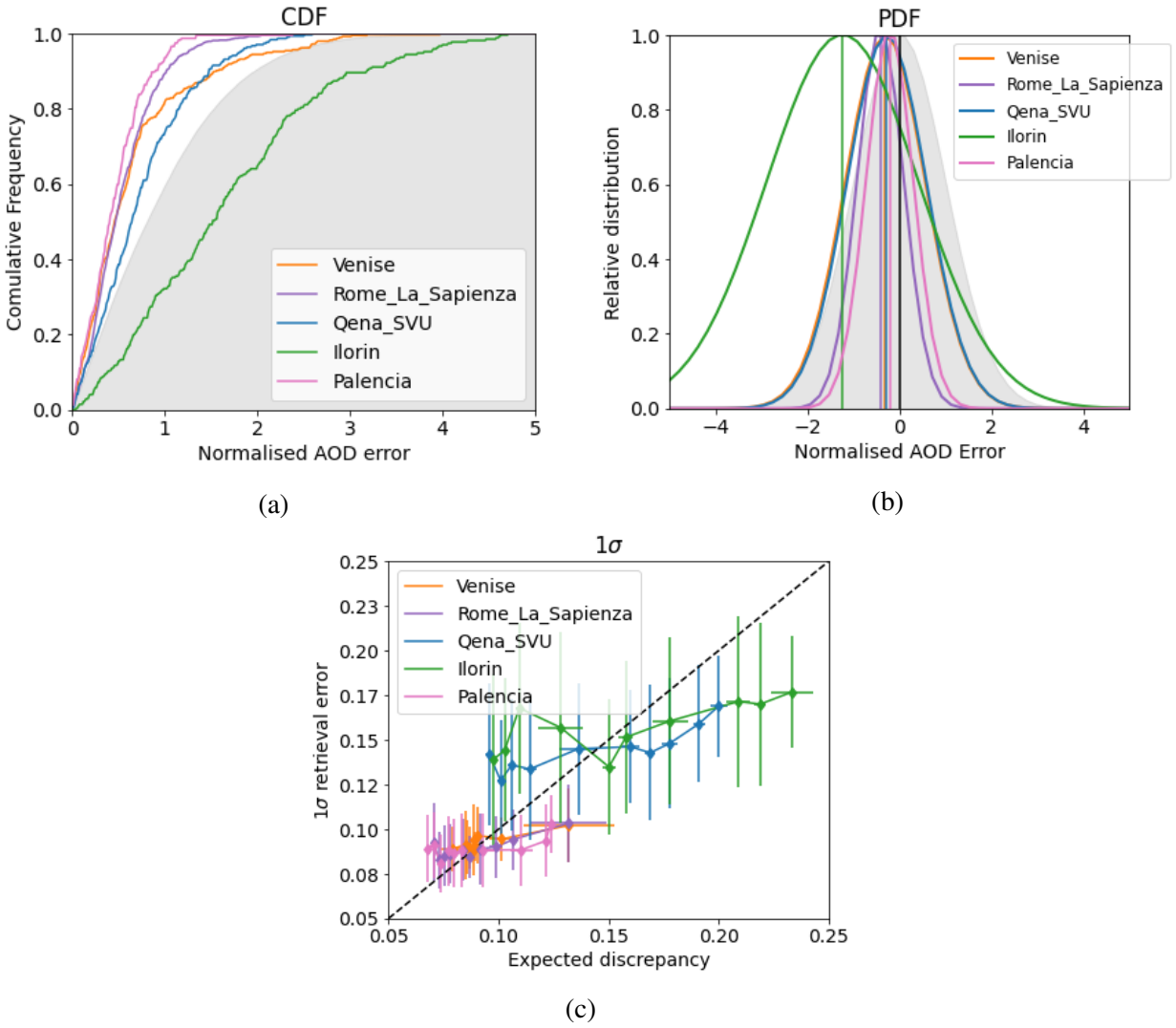


Figure 13: Normalised error CDF (a), PDF (b) and expected AOD discrepancy against percentiles of absolute AOD retrieval error (c) over selected AERONET stations. The shaded grey area represent the ideal case where the normalised AOD error can be approximated as a Gaussian distribution with mean 0 and variance 1.

## 3.3 Aerosol-cloud interactions

Aerosol research is of fundamental importance for climate studies due to high uncertainty associated to their direct and indirect effects. Measurements from satellite-based remote sensing techniques remain the primary source of global data to study aerosol-cloud interactions; however, concerns about possible artefacts in both the aerosol and cloud products still persist (Boucher et al. 2013). Cloud contamination in aerosol products could lead to an enhancement of the measured top-of-atmosphere (TOA) bidirectional reflectance factor (BRF) and in turn to an overestimated AOD. However, aerosol particles near clouds become more hydrating and swell in size, resulting in increased AOD (Quaas et al. 2010). It is therefore expected to see an increase in aerosol size and OD in the vicinity of clouds. At the same time, aerosols affect cloud properties acting as Cloud Condensation Nuclei (CCN) and

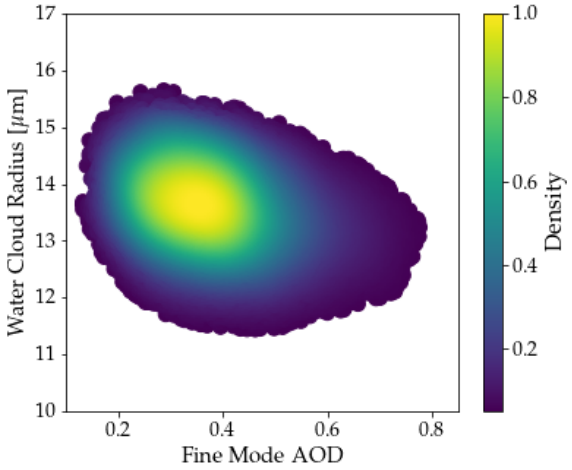


Figure 14: Density plot between the water cloud radius (y axis) and the fine mode AOD (x axis) during May 2020 over Europe obtained with the CISAR algorithm applied to SEVIRI observations.

increase the number of cloud droplet concentration, while decreasing the droplet size for fixed water content in liquid clouds (Twomey 1974). Thanks to the innovative CISAR AOD/COD combined product it is possible to observe the effects of aerosol swelling near clouds as well as the first indirect effect on liquid clouds. For this demonstration study, one month of data (May 2020) over Europe is considered. To observe the first indirect aerosol effect on cloud, the CISAR retrieval is filtered to only consider water clouds. These clouds are expected to be lower in the atmosphere than the ice clouds and therefore interact more likely with aerosols. The mean cloud radius is calculated as a weighted mean of the radius of each cloud vertex in the CISAR solution space, weighted by the retrieved OD associated to each vertex (similarly to Eq. 2 in Luffarelli et al. 2022). The relationship between the retrieved average water cloud radius and the FM AOD retrieved by CISAR from SEVIRI observations in the VIS0.6 band is shown in Figure 14. As expected, it can be seen that the cloud droplets' size decreases as the aerosol load associated to fine particles increases.

Similarly, the relationship between the aerosol radius and water cloud AOD has been observed, using

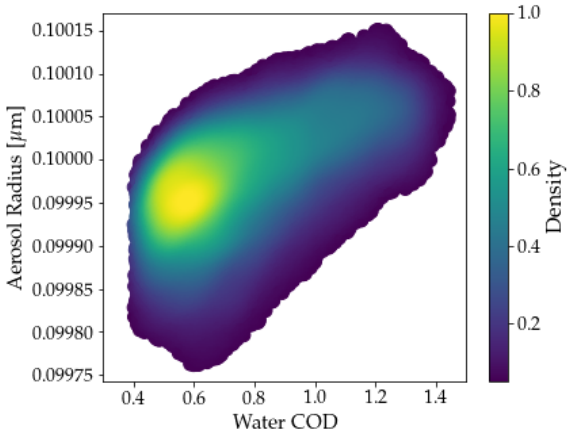


Figure 15: Density plot between the water cloud radius (y axis) and the fine mode AOD (x axis) during May 2020 over Europe obtained with the CISAR algorithm applied to SEVIRI observations.

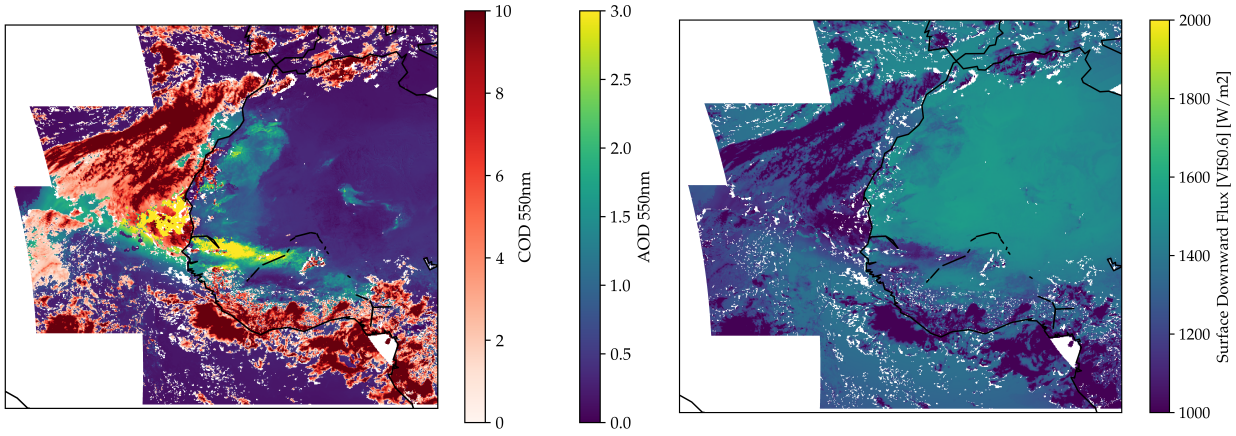


(a) (b)

Figure 16: Combined AOD/COD product at 550 nm (16a) and surface downward flux in the VIS0.6 band (16b) retrieved with the CISAR algorithm applied to SEVIRI observations on-board MSG1 and MSG4 during June16th, 2020.

the same dataset as above. Figure 15 shows that the aerosol radius increases as the water cloud OD increases, as expected given the aerosol swelling in humid environment. These results are extremely encouraging as, although obtained from a limited dataset and the simple characterisation of the atmospheric solution space (Govaerts and Luffarelli 2018, Luffarelli and Govaerts 2019), show that CISAR retrieves correctly the changes in both aerosol and cloud particles in cloudy environments.

## 3.4 AOD/COD impact on surface downward flux

Downward short-wave radiation is a fundamental quantity for a wide variety of applications, such as climate studies and terrestrial ecological and hydrological modelling. Compared to ground-observations or numerical data reanalysis, remote sensing techniques offer the advantages of global coverage and higher spatial resolutions (Yu et al. 2021). The possibility of processing all-sky pixels provides an increased spatial continuity in the downward short-wave radiation product. Figure 16 show an example of such combined product, where the surface downward fluxes are retrieved on all-skies. Both images are retrieved from SEVIRI observations during June 2020 over the Western coast of Africa, where a large and tick dust storm, named Godzilla, originated in this area, and moved over thousands towards the Caribbean islands. During this extreme event, the surface downward irradiance is here retrieved continuously in clear sky and in presence of thin clouds, and it decreases with increasing OD. The decrease in surface downward fluxes with increasing OD can be observed in Figure 17, showing the density plot between the two quantities obtained from the sub-dataset over May 2020 over Europe used in Section 3.3. In particular, the impact of the tick dust storm on the surface downward fluxes is analysed in Section 4.1.

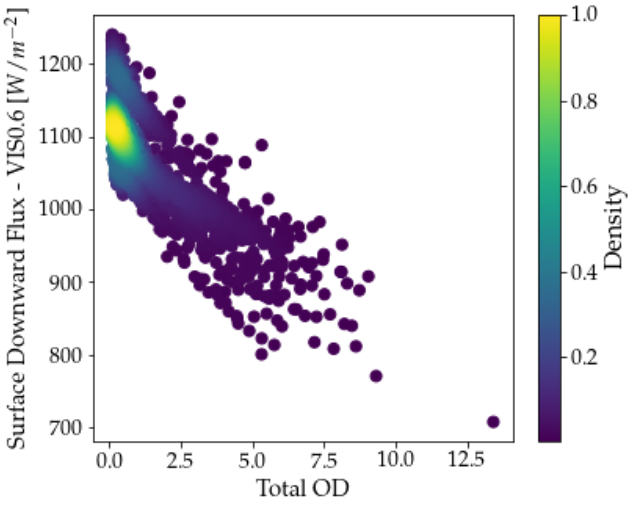


Figure 17: Density plot between the surface downward fluxes in the SEVIRI VIS0.6 band (y axis) and the total OD retrieved at $0.55$ um (x axis) during May 2020 over Europe obtained with the CISAR algorithm applied to SEVIRI observations.

# 4 Case Study

## 4.1 The Godzilla dust storm

Of particular interest for evaluation purposes is the Godzilla dust storm, originating in June in the Sahara region, and moving towards the Caribbean islands during June 2020. The evaluation against MODIS and CAMS data shows good agreement in terms of spatial distribution of the dust plume (Figure 18). The CISAR product retrieves higher AOD than the CAMS simulations over the dust plume; however the CAMS product tends to underestimate the maximum value of the dust AOD (ECMWF Copernicus report, 2021). The position of the clouds in the CISAR product is in good agreement with the RGB image obtained from MODIS MOD09GA observations (Vermote 2021). Although the position of the dust plume is consistent with the CAMS dataset, both CISAR and MODIS products present some limitation in the continuity of the product along the coast, between the land and ocean product. The CISAR algorithm also implements spatial constraints; however, this can only be applied when some overlap is present between two consecutive accumulation periods (Luffarelli et al. 2022). The overlap is normally implemented for longer accumulation periods, e.g. longer than 10 days, as the assumption on the invariability of the surface reflectance becomes weaker during longer time windows and it is necessary to perform a new retrieval with a shorter frequency. In the framework of the DUST2MSG project, the accumulation periods are set to a 5-days temporal window and to do not overlap. Although introducing an overlap could potentially improve the continuity of the aerosol product, a thread-off is introduced as the computational time needed to process the whole dataset would increases proportionally with the overlap.

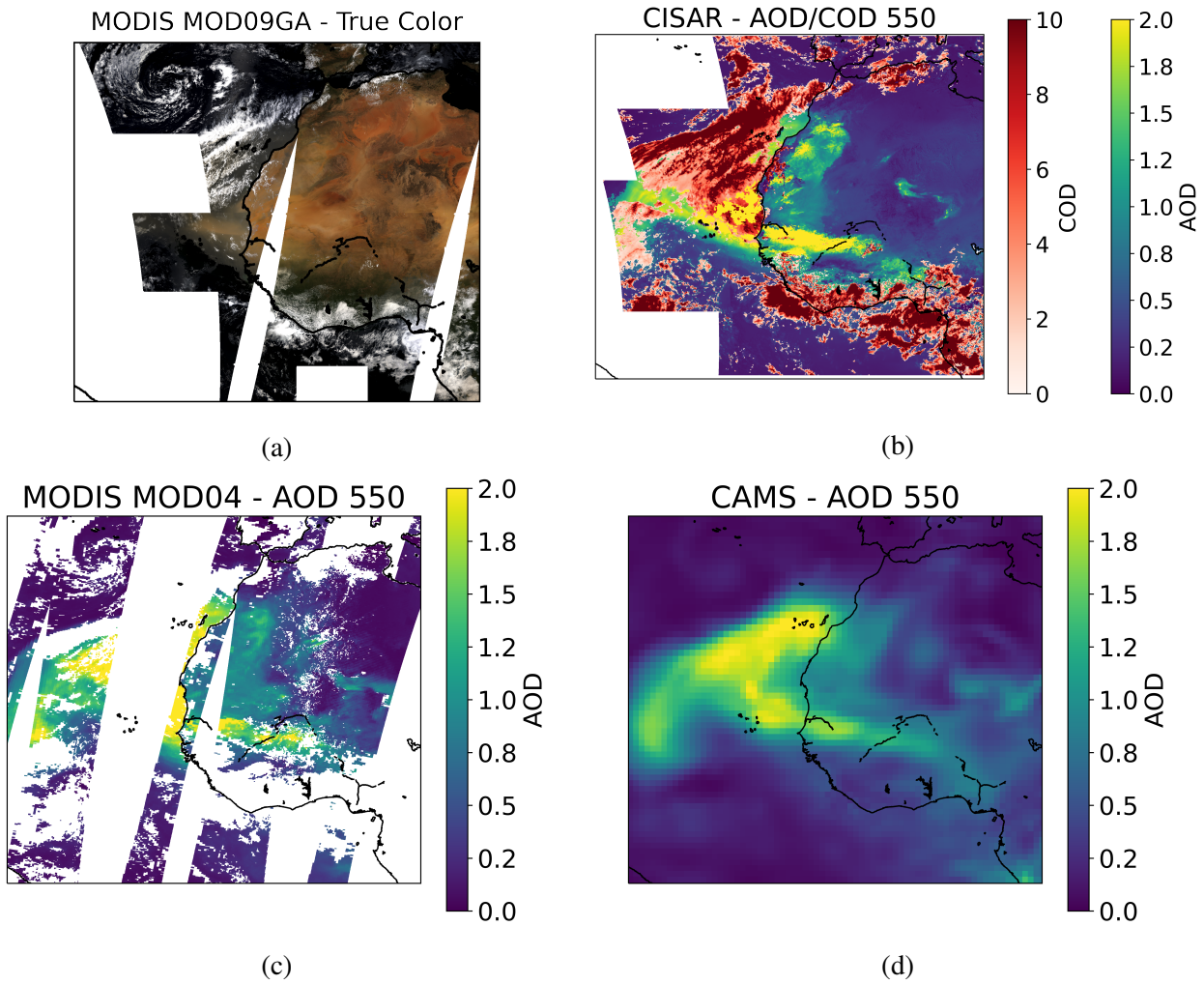


Figure 18: Products over over the West African coast during June 16th, 2020: true color image obtained from the MODIS MOD09GA product (a); SEVIRI/CISAR combined AOD/COD retrieval (b), MODIS/MAIAC MCD19A2 product (c) and CAMS dataset (d).

The spatial coverage of the aerosol product is strongly improved with respect to the MODIS product, and continuity between the aerosol and cloud product is provided by the CISAR combined AOD/COD product, both over land and over ocean. The continuous AOD-COD product could provide significant support in aerosol-cloud interactions studies, as discussed in Section 3.3.

The tick Godzilla dust storm is correctly identified as coarse mode in the CISAR retrieval, as the FMF reaches values lower than 0.1. The FMF retrieved by CISAR is qualitatively compared with the MOD04 product (Figure 19). The availability of MODIS derived FMF is however limited over land. The two products show similar spatial distribution of the FMF, with larger contribution of the FM to the total AOD towards Southern Europe. Some differences are observed at the coast of Central Africa, where MAIAC/MODIS presents larger value of FMF with respect to CISAR applied to SEVIRI. However, some thin clouds are present in this area (see Figure 18a), which could lead to some fine-mode overestimation in the MODIS product (Smirnov et al. 2018). Finally, it should be noted that this evaluation should be considered only qualitatively, especially over land, where little confidence is placed in the FMF product from MODIS (Levy et al. 2010).

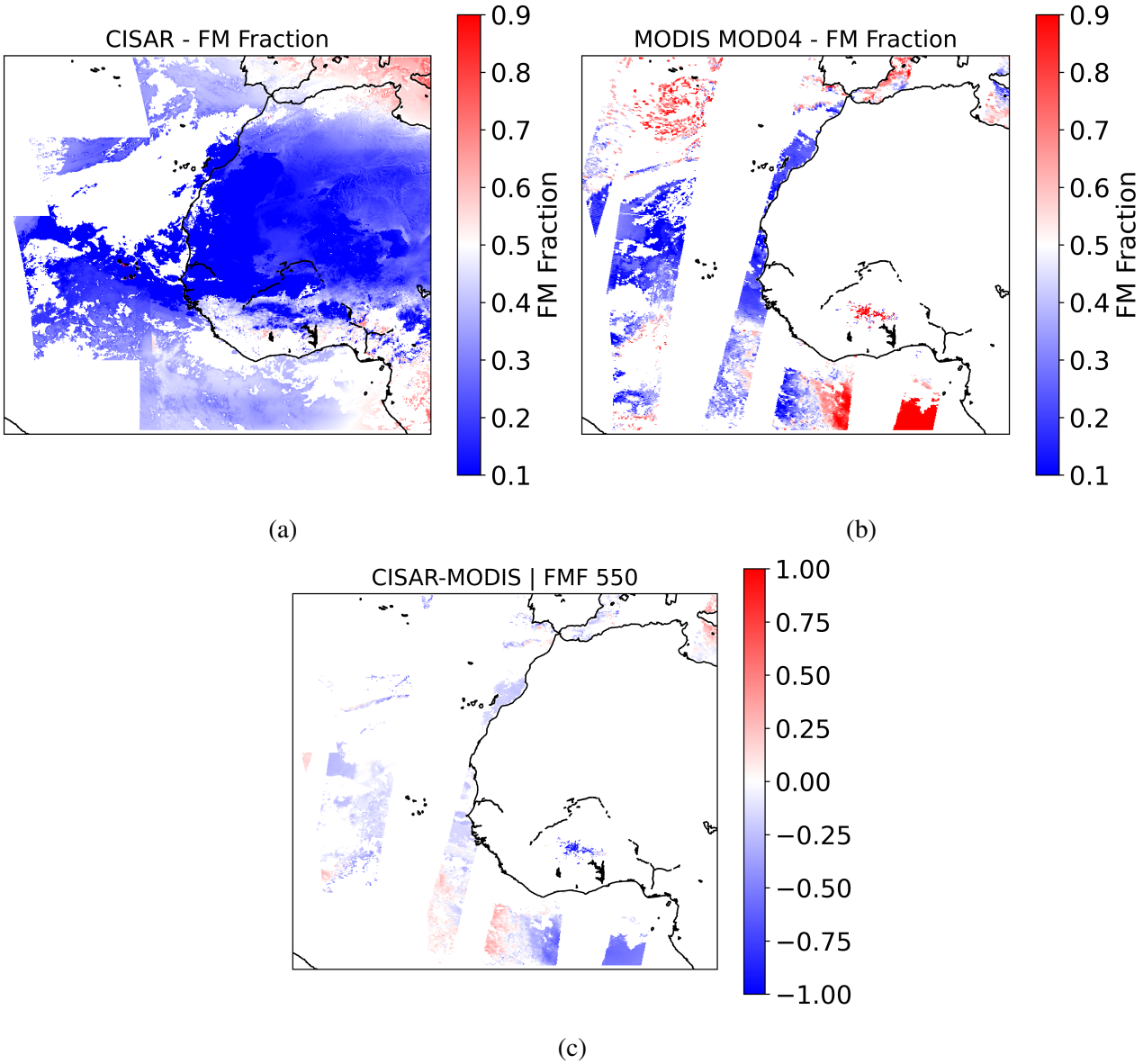


Figure 19: Fine Mode Fraction retrieved from the CISAR algorithm applied to SEVIRI (19a), from MAIAC applied to MODIS (19b) and the associated bias (19c).

The CISAR algorithm also provides the spectral Surface Downward Irradiance [W/m2]. It is interesting to observe the impace of the Godzilla dust storm on the downward irrandiance, as shown in the time series in Figure 20. The latter shows the daily average of the coarse mode AOD and the surface downward fluxes retrieved. These quantities appear to be anti-correlated, with the solar radiation reaching the Earth's surface decreasing as the AOD increases. This is in line with the expected outcome, as discussed in Section 3.4.

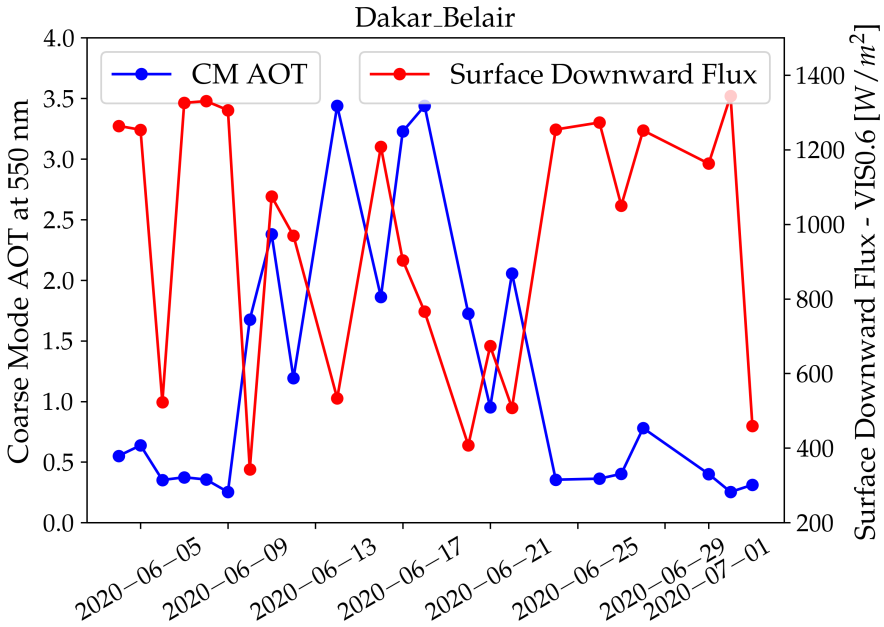


Figure 20: Time series during June 2020 of the daily average of the Coarse Mode AOT (left y axis, blue line) and the surface downward irradiance (right y axis, red line) retrieved by CISAR.

# 5 Known issues and algorithm limitations

## 5.1 Corrupted SEVIRI image

During May 9th 2020, in the hourly time slot between 2pm and 3pm, the CISAR product shows a horizontal line in the Northern part of the Sahara region Figure(21b). This artefact is however present in the native SEVIRI product (Figure 21a) and is therefore not due to the CISAR algorithm's inversion.

## 5.2 Ocean color

One of the limitation of the surface albedo calculation over water with the CISAR algorithm, is that the chlorophyll amount in the ocean is considered constant; consequently, CISAR is not able to retrieve changes in the ocean color, which might result in artefacts in the AOD retrieval. Future improvements of the CISAR algorithm might include customisable chlorophyll concentration.

## 5.3 Snow pixels

The surface spectral constraints currently implemented in the CISAR algorithm exclude the processing of snow covered surfaces. Future improvements of the CISAR algorithm might include the implementation of new spectral constraints over snow pixels.

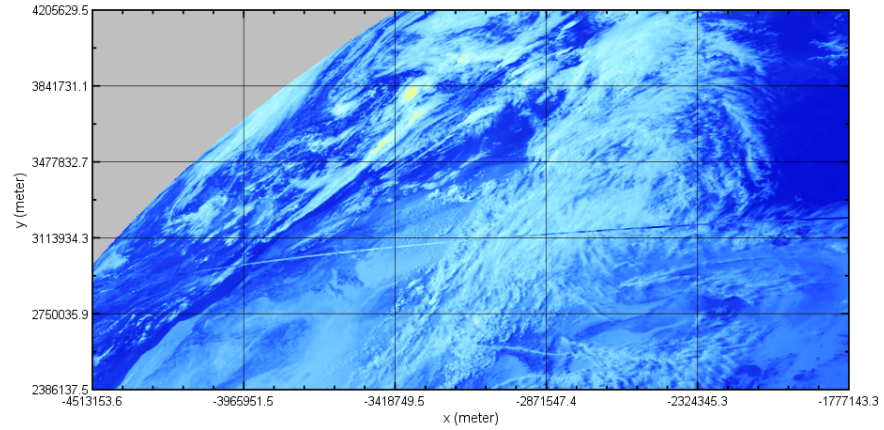


(a)

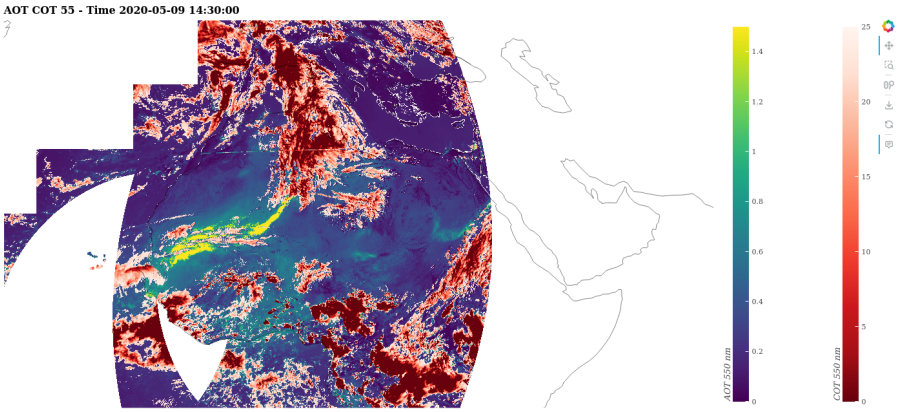


(b)

Figure 21: Level 1.5 image acquired by MSG1 in the VIS0.6 band (a) and associated CISAR AOD/COD retrieval at 0.55 um (b) during May 9th 2020.

# 6 Summary

This document report the results from the validation of the DUST2MSG User Products obtained with the CISAR algorithm from SEVIRI on board MSG1 and MSG4 during March-August 2020. The CISAR products have been evaluated against ground-based measurements, cross-sensor products and model datasets.

The overall evaluation against AERONET V3 L2.0 shows a correlation of 0.72 and a RMSE of 0.12. More than 75% of the retrievals satisfy the GCOS Threshold requirements. This percentage increases as the observations as filtered according the quality indicator, allowing the users to chose the level of accuracy best suited for their application. The percentage of points outside the GCOS requirements is larger at brighter targets, such as in the Sahara region (Figure 2). Also, most of the retrieval not satisfying the requirements are associated with a scattering angle in the range of 100°-140° (Figure 3), which is associated to the minimum of the aerosols phase function. Finally, among the retrieval which appear to be overestimated with respect to AERONET, 54% are associated to an AERONET AOD lower than 0.2, suggesting residual cloud contamination. Indeed, the occurrence of overestimated retrieval decreases if AERONET collocation with at least 4 observations per hour are considered. The cloud contamination can affect from satellite retrieval differently than ground measurements given the difference spatial resolution. The temporal evolution of the AOD retrieved by CISAR is consistent with the AERONET dataset, despite the above mentioned issue of over-estimation. CISAR uncertainties are also evaluated exploiting the AERONET dataset as reference, showing a large improvement compared to Sayer et al. 2020.

The CISAR combined AOD/COD product showed good potential in observing aerosol-cloud mutual effects, such as the first indirect effect and the aerosol swelling (Section 3.3). Also, such combined product provides the spectral surface downward fluxes with improved spatial coverage, as all-sky observations are processed. This also allows to assess the impact of the total OD on the solar irradiance at the surface. The anti-correlation between OD and surface downward fluxes is also observed during the Godzilla dust storm (Section 4.1). During such an extreme event, CISAR retrieves the position of the dust plume in good spatial agreement with both CAMS and MODIS datasets, as well as the position of clouds (Figure 18). The tick dust plume is correctly identified as coarse mode in the CISAR retrieval.

To conclude, this validation exercise shows good agreement with external reference datasets obtained from different techniques, and it highlight the potential of the combined AOD/COD product to observe mutual aerosol-cloud effect at large scale from satellite observations.

# References

100:2008, G. . J. (2008). Evaluation of Measurement Data—Guide to the Expression of the Uncertainty in Measurement. Technical Report JCGM 100:2008 GUM 1995 with minor corrections.

Boucher, O., D. Randall, P. Artaxo, C. Bretherton, G. Feingold, P. Forster, V.-M. Kerminen, Y. Kondo, H. Liao, U. Lohmann, P. Rasch, S. Satheesh, S. Sherwood, B. Stevens, and X. Zhang (2013). Clouds and aerosols. in: Climate change 2013: The physical science basis. contribution of working group i to the fifth assessment report of the intergovernmental panel on climate change. Technical report.

Fougnie, B., J. Chimot, M. Vázquez-Navarro, T. Marbach, and B. Bojkov (2020). Aerosol retrieval from space – how does geometry of acquisition impact our ability to characterize aerosol properties. Journal of Quantitative Spectroscopy and Radiative Transfer 256, 107304.

Giles, D. M., B. N. Holben, T. F. Eck, A. Smirnov, A. Sinyuk, J. Schafer, M. G. Sorokin, and I. Slutsker (2017, December). Aerosol Robotic Network (AERONET) Version 3 Aerosol Optical Depth and Inversion Products. In AGU Fall Meeting Abstracts, Volume 2017, pp. A11O–01.

Govaerts, Y. and M. Luffarelli (2018, December). Joint retrieval of surface reflectance and aerosol properties with continuous variation of the state variables in the solution space – Part 1: theoretical concept. Atmospheric Measurement Techniques 11(12), 6589–6603.

Inness, A., M. Ades, A. Agustí-Panareda, J. Barré, A. Benedictow, A.-M. Blechschmidt, J. J. Dominguez, R. Engelen, H. Eskes, J. Flemming, V. Huijnen, L. Jones, Z. Kipling, S. Massart, M. Parrington, V.-H. Peuch, M. Razinger, S. Remy, M. Schulz, and M. Suttie (2019, March). The CAMS reanalysis of atmospheric composition. Atmospheric Chemistry and Physics 19(6), 3515–3556. Publisher: Copernicus GmbH.

Kinne, S., D. O'Donnel, P. Stier, S. Kloster, K. Zhang, H. Schmidt, S. Rast, M. Giorgetta, T. F. Eck, and B. Stevens (2013, December). MAC-v1: A new global aerosol climatology for climate studies. Journal of Advances in Modeling Earth Systems 5(4), 704–740.

Levy, R. C., L. A. Remer, R. G. Kleidman, S. Mattoo, C. Ichoku, R. Kahn, and T. F. Eck (2010, November). Global evaluation of the Collection 5 MODIS dark-target aerosol products over land. Atmospheric Chemistry and Physics 10(21), 10399–10420. Publisher: Copernicus GmbH.

Luffarelli, M. and Y. Govaerts (2019, February). Joint retrieval of surface reflectance and aerosol properties with continuous variation of the state variables in the solution space – Part 2: application to geostationary and polar-orbiting satellite observations. Atmospheric Measurement Techniques 12(2), 791–809.

Luffarelli, M., Y. Govaerts, and A. Damman (2016, May). ASSESSING HOURLY AEROSOL PROPERTY RETRIEVAL FROM MSG/SEVIRI OBSERVATIONS IN THE FRAMEWORK OF AEROSOL_CCI2. ESA.

Luffarelli, M., Y. Govaerts, and L. Franceschini (2022, May). Aerosol Optical Thickness Retrieval in Presence of Cloud: Application to S3A/SLSTR Observations. Atmosphere 13(5), 691. Number: 5 Publisher: Multidisciplinary Digital Publishing Institute.

Lyapustin, A. and Y. Wang (2018). Modis multi-angle implementation of atmospheric correction (maiac) data user's guide. Technical Report V2.0, LP DAAC.

Lyapustin, A., Y. W. (2018). Mcd19a2 modis/terra and aqua land aerosol optical depth daily l2g global 1km sin grid v006. Technical report, LP DAAC.

O'Neill, N. T., T. F. Eck, A. Smirnov, B. N. Holben, and S. Thulasiraman (2003). Spectral discrimination of coarse and fine mode optical depth. Journal of Geophysical Research: Atmospheres 108(D17). _eprint: https://onlinelibrary.wiley.com/doi/pdf/10.1029/2002JD002975.

Quaas, J., B. Stevens, P. Stier, and U. Lohmann (2010). Interpreting the cloud cover – aerosol optical depth relationship found in satellite data using a general circulation model. Atmospheric Chemistry and Physics 10(13), 6129–6135.

Remer, L. A., S. Mattoo, R. C. Levy, A. Heidinger, R. B. Pierce, and M. Chin (2012, July). Retrieving aerosol in a cloudy environment: aerosol product availability as a function of spatial resolution. Atmospheric Measurement Techniques 5(7), 1823–1840. Publisher: Copernicus GmbH.

Rodgers, C. D. (2000). Inverse methods for atmospheric sounding. Series on Atmospheric Oceanic and Planetary Physics. World Scientific.

Sayer, A. M., Y. Govaerts, P. Kolmonen, A. Lipponen, M. Luffarelli, T. Mielonen, F. Patadia, T. Popp, A. C. Povey, K. Stebel, and M. L. Witek (2020, February). A review and framework for the evaluation of pixel-level uncertainty estimates in satellite aerosol remote sensing. Atmospheric Measurement Techniques 13(2), 373–404.

Smirnov, A., T. B. Zhuravleva, M. Segal-Rosenheimer, and B. N. Holben (2018, February). Limitations of AERONET SDA product in presence of cirrus clouds. Journal of Quantitative Spectroscopy and Radiative Transfer 206, 338–341.

Twomey, S. (1974, December). Pollution and the planetary albedo. Atmospheric Environment (1967) 8(12), 1251–1256.

Vermote, E., R. W. (2021). Modis/terra surface reflectance daily l2g global 1km and 500m sin grid v061. Technical report, LP DAAC.

WMO (2022). GCOS, 245. The 2022 GCOS ECVs Requirements (GCOS 245). Geneva: WMO.

Yu, Y.-C., J. Shi, T. Wang, H. Letu, and C. Zhao (2021, October). All-sky total and direct surface Shortwave Downward Radiation (SWDR) estimation from satellite: Applications to MODIS and Himawari-8. International Journal of Applied Earth Observation and Geoinformation 102, 102380.